

Principled Argo Modeling using Vecchia-based Gaussian Processes

Nian Liu ^{*} Jian Cao [†]

Abstract

Argo is an international program that collects temperature and salinity observations in the upper two kilometers of the global ocean. Most existing approaches for modeling Argo temperature rely on spatial partitioning, where data are locally modeled by first estimating a prescribed mean structure and then fitting Gaussian processes (GPs) to the mean-subtracted anomalies. Such strategies introduce challenges in designing suitable mean structures and defining domain partitions, often resulting in ad hoc modeling choices. In this work, we propose a one-stop Gaussian process regression framework with a generic spatio-temporal covariance function to jointly model Argo temperature data across broad spatial domains. Our fully data-driven approach achieves superior predictive performance compared with methods that require domain partitioning or parametric regression. To ensure scalability over large spatial regions, we employ the Vecchia approximation, which reduces the computational complexity from cubic to quasi-linear in the number of observations while preserving predictive accuracy. Using Argo data from January to March over the years 2007–2016, the same dataset used in prior benchmark studies, we demonstrate that our approach provides a principled, scalable, and interpretable tool for large-scale oceanographic analysis.

Keywords: automatic relevance determination, benchmark study, non-parametric spatio-temporal regression, sparse inverse Cholesky factor

^{*}Department of Mathematics, University of Houston, Email: nliu9@central.uh.edu

[†]Department of Mathematics, University of Houston, Email: jcao21@central.uh.edu

1 Introduction

The international Argo program (Argo, 2000) provides global subsurface ocean observations using autonomous floats that drift with ocean currents. Each float measures temperature, pressure, and salinity as it ascends from approximately 2 km depth to the surface. In this paper, pressure and depth are used interchangeably, as a pressure of 1 decibar (dbar) roughly corresponds to a depth of 1 meter. A complete vertical set of measurements from a single float within a short time window is referred to as a profile, which approximately corresponds to one horizontal location (longitude and latitude). An observation denotes a single measurement (e.g., temperature or salinity) at a specific depth within a profile. Every ten days, floats transmit their profile data via satellite to the global Argo database. The resulting dataset covers vast spatial and temporal scales, offering rich information for ocean state estimation and prediction. However, effective analysis of these data requires spatio-temporal modeling that accounts for complex correlations across longitude, latitude, depth, and time—posing significant methodological and computational challenges.

A large body of work has addressed the modeling of temperature and salinity in Argo data. Most approaches adopt a two-stage modeling scheme, consisting of a parametric mean-field estimation followed by stochastic modeling of the residual (anomaly) field. In the first stage, a mean structure is typically fitted via weighted least squares; in the second, a Gaussian process (GP) or similar stochastic model captures the residual spatial-temporal variability. Representative works include Roemmich and Gilson (2009), Kuusela and Stein (2018), Hu et al. (2024), and Yarger et al. (2022). Roemmich and Gilson (2009) divided the depth range into bins and locally fitted monthly mean fields using weighted least squares, followed by objective analysis (Bretherton et al., 1976; Roemmich, 1983) of the anomalies. Kuusela and Stein (2018) interpolated temperatures onto three fixed pressure levels, estimated the Roemmich–Gilson (RG) mean field, and modeled anomalies using moving-window GP regression with a spatio-temporal covariance. Hu et al. (2024) used unweighted local windows to fit the RG mean field before applying the same GP model as Kuusela and

Stein (2018). Yarger et al. (2022) instead estimated functional mean fields and introduced a spatio-temporal functional kriging model to jointly predict temperature and salinity as functions of depth. These two-stage approaches, while effective, can be suboptimal relative to a single-stage maximum likelihood estimation (MLE) when computationally feasible. Moreover, their uncertainty quantification applies only to the residual field rather than the original spatio-temporal response. Finally, many existing methods rely on subjective spatio-temporal domain partitioning to make computation feasible, an approach that may induce overfitting and discontinuities across partition boundaries.

Several other studies employed iterative optimization for Argo data modeling, which are generally less efficient than direct likelihood-based methods. For instance, Gray and Riser (2015) decomposed an Argo variable into large-scale, small-scale, and noise components and iteratively estimated these using generalized least squares. Korte-Stapff et al. (2022) jointly modeled temperature and salinity as a sum of a parametric mean and basis-function expansions with latent coefficients, estimated via an expectation–maximization (EM) algorithm. Although flexible, such iterative procedures are typically not scalable with the number of measurements used for training. Multivariate extensions have also been proposed, often using multivariate GPs. For example, Bolin and Wallin (2020) and Yarger et al. (2023) respectively developed SPDE-based and spectral-based multivariate Matérn models to jointly model temperature anomalies at different depths, while Salvana et al. (2025) introduced multivariate nonstationary GPs based on differential operators. Yarger and Bhadra (2023) modeled temperature, salinity, and oxygen in the Southern Ocean by locally estimating a spatially varying mean and subsequently applying a stationary Gaussian model to the anomalies.

In this paper, we propose a one-stop Gaussian process regression for modeling Argo variables using a principled, likelihood-based approach. Motivated by the prevalence of two-stage anomaly-based modeling, our study revisits the question of whether a direct single-stage GP without a prescribed mean structure can achieve competitive performance. As a

flexible nonparametric model, a GP can often learn the underlying spatial-temporal patterns without requiring complex parametric means, especially when physical knowledge is unknown or incomplete. We demonstrate that a single-stage GP with a generic covariance structure performs comparably or better than existing two-stage approaches, while avoiding ad hoc mean specification and domain partitioning. For empirical evaluation, we focus on the temperature field, the most widely studied Argo variable in the literature.

A major barrier to single-stage GP modeling is computational scalability. For n observations, standard GP inference requires the Cholesky factorization of an $n \times n$ covariance matrix, which incurs $\mathcal{O}(n^3)$ floating-point operations, prohibitive for large-scale datasets such as Argo. Numerous scalable approximations have been developed, including covariance tapering (Furrer et al., 2006; Kaufman et al., 2008; Du et al., 2009), composite likelihood methods (Varin et al., 2011; Bevilacqua et al., 2012; Eidsvik et al., 2014), Gaussian Markov random field approximations (Rue and Held, 2005; Lindgren et al., 2011), and multi-resolution approaches (Nychka et al., 2015; Katzfuss, 2017). Here we employ the Vecchia approximation (Vecchia, 1988; Katzfuss and Guinness, 2021), which imposes an ordered conditional independence assumption yielding a sparse inverse Cholesky factor of the covariance matrix. Theoretical and empirical studies (Stein et al., 2004; Datta et al., 2016; Guinness, 2018; Finley et al., 2019; Schäfer et al., 2021; Cao et al., 2022) have shown that this approximation preserves predictive accuracy while reducing computational complexity to quasi-linear in n . Guinness (2021) further derived efficient gradient and Fisher information computations under the Vecchia framework, implemented in the R package `GpGp`. Although Guinness (2021) briefly illustrated this approach using a subset of Argo temperature data, they did not provide a direct comparison against two-stage methods. The present work fills this gap by systematically evaluating the one-stop GP regression with Vecchia approximation against two established approaches.

The remainder of the paper is organized as follows. Section 2 reviews two representative benchmark methods. Section 3 details the Gaussian process model and the Vecchia approx-

imation. Section 4 presents empirical comparisons using Argo temperature data. Section 5 concludes with discussions and future directions.

2 Representative methods in the literature

Kuusela and Stein (2018) and Yarger et al. (2022) represent two prominent approaches in the literature for modeling the Argo dataset. Both methods first estimate local mean fields and then fit stationary Gaussian processes (GPs) to the mean-subtracted anomaly fields. To ensure computational feasibility given the large data volume, they partition the three-dimensional domain defined by longitude, latitude, and time, and assume independence across partitions. However, such partition-wise independence can introduce instability, as different choices of partition sizes or boundaries may lead to substantial variations in the kriging results. In addition, the two methods employ distinct prescribed regression functions for the mean structures, which are not necessarily physically grounded and may be more prone to model misspecification than data-driven, nonparametric alternatives. Finally, temperature prediction is obtained by adding the estimated mean to the kriging predictor of the anomaly, potentially resulting in discontinuities across partition boundaries.

Kuusela and Stein (2018) structure the mean based on the Roemmich-Gilson (RG) function (Roemmich and Gilson, 2009; Ridgway et al., 2002), which includes linear and quadratic functions of the spatial coordinates and trigonometric functions of the temporal coordinate. Specifically, the RG mean field is

$$\begin{aligned} \mu(l, L, p, d) = & \beta_0 + \beta_1 l + \beta_2 L + \beta_3 p + \beta_4 l^2 + \beta_5 L^2 + \beta_6 p^2 \\ & + \sum_{k=1}^6 \gamma_k \sin\left(2\pi k \frac{d}{365.25}\right) + \sum_{k=1}^6 \delta_k \cos\left(2\pi k \frac{d}{365.25}\right), \end{aligned} \quad (1)$$

where $\{\beta_k\}_{k=0}^6$, $\{\gamma_k\}_{k=1}^6$ and $\{\delta_k\}_{k=1}^6$ are parameters to be estimated, l is latitude, L is longitude, p is pressure, and d is the day of the year. Roemmich and Gilson (2009) divided

the pressure range of 0-2000 dbar into 58 bins and locally fitted a monthly mean field for each bin at each horizontal grid point using weighted least-squares based on 300 nearest measurements. When the profile density is low, however, this approach may lead to incorrect mean estimation due to the incorporation of far-away measurements. Kuusela and Stein (2018) adopt the strategy of Roemmich and Gilson (2009) and assign weights inversely proportional to the distance d_{RG}

$$d_{\text{RG}}(\mathbf{s}, \mathbf{s}_g) = \sqrt{(l - l_g)^2 + (L - L_g)^2 + \frac{5(200\text{km} \cdot (p - p_g))^2}{p^2 + p_g^2}}, \quad (2)$$

where we use \mathbf{s} to denote the triplet of latitude, longitude, and depth, i.e., $\mathbf{s} = (l, L, p)$. $\mathbf{s}_g = (l_g, L_g, p_g)$ and \mathbf{s} are the triplets corresponding to a grid point (i.e., a reference location) and a measurement used in the estimation of the local mean function at the grid point, respectively. Three pressure levels are used in Kuusela and Stein (2018), namely 10 dbar, 300 dbar, and 1500 dbar, which have depth bands of width 10 dbar, 20 dbar, and 100 dbar, respectively. At each depth level, the local mean structures described in Equation (1) were estimated independently at each grid point using 300 measurements, consisting of 100 observations each from the target pressure bin and its two adjacent bins, and for a large 2D horizontal grid with a band-width of $1/6^\circ$. The mean-subtracted anomalies were then modeled using a moving-window Gaussian process (GP), where GPs were fitted independently within spatial windows of $20^\circ \times 20^\circ$ and temporal ranges of either one month or three months over the years 2007–2016. The spatial window moved with a resolution of $1^\circ \times 1^\circ$. Each locally fitted GP employed a spatio-temporal exponential covariance function with an automatic relevance determination (ARD) structure (Neal, 2012):

$$C(\Delta l, \Delta L, \Delta d) = \sigma^2 \exp \left(-\sqrt{\left(\frac{\Delta l}{r_l}\right)^2 + \left(\frac{\Delta L}{r_L}\right)^2 + \left(\frac{\Delta d}{r_d}\right)^2} \right), \quad (3)$$

where $\sigma^2 > 0$ is the marginal variance; Δl , ΔL , and Δd are the differences in latitude,

longitude and time (days); r_l , r_L , and r_d are separate ranges for longitude, latitude, and day of the year, respectively. Posterior inference is performed locally, based on the ordinary kriging within the partition where the point for prediction is located.

Yarger et al. (2022) proposed a spatio-temporal functional kriging approach that jointly models the temperature and salinity in the Argo dataset across depth. Denote by $W_{i,j}$ an Argo variable (temperature or salinity) measured at the j -th depth in the i th profile, noticing that the full set of covariates indexing a measurement is $(l_i, L_i, p_{i,j}, d_i, y_i)$, where (l_i, L_i) is the profile-dependent longitude-latitude pair, $p_{i,j}$ is the measurement-specific depth, d_i and y_i are the profile-dependent temporal coordinates, namely, the day of the year and the year number, respectively. The two-stage modeling approach in Yarger et al. (2022) is based on the decomposition:

$$W_{i,j} = \mu(l_i, L_i, p_{i,j}, d_i, y_i) + \xi(l_i, L_i, d_i, y_i, p_{i,j}) + \epsilon_{i,j}, \quad (4)$$

where μ is a deterministic mean function, ξ is a zero-mean stochastic process, and $\epsilon_{i,j}$ is a white noise that models the measurement error. The mean field μ includes linear and quadratic terms of the spatio-temporal coordinates:

$$\mu(l, L, p, d, y) = \beta_{0,y}(p) + \beta_1(p)l + \beta_2(p)L + \beta_3(p)l^2 + \beta_4(p)L^2 + \beta_5(p)lL + \beta_6(p)d + \beta_7(p)d^2, \quad (5)$$

where $\beta_{0,y}$ and $\{\beta_k\}_{k=1}^7$ are smooth functions with the support over the whole depth range and finite second-order moments. For each horizontal grid point at a 1° resolution, the mean function is estimated using profiles located within 900 kilometers of the grid point, collected from January to March over the years 2007–2016. The coefficients $\beta_{0,y}$ and $\{\beta_k\}_{k=1}^7$ in the mean function (5) are obtained via weighted least squares, with weights determined by the spatio-temporal distances between the selected profiles and the target grid point.

To obtain the anomaly process $\xi(\cdot)$, each $W_{i,j}$ is demeaned by subtracting the value of the local mean function of its nearest grid point, evaluated at the corresponding pressure

level $p_{i,j}$. The anomaly ξ is then modeled as

$$\xi(l_i, L_i, d_i, y_i, p) = \sum_{k=1}^{10} Z_k(l_i, L_i, d_i, y_i), \phi_k(p), \quad (6)$$

where $\{Z_k\}_{k=1}^{10}$ are ten independent Gaussian processes with exponential covariance functions that define the coefficients of $\{\phi_k\}_{k=1}^{10}$, a set of deterministic orthonormal basis, each being a linear combination of a univariate B-spline basis. The anomaly process, including the variance of the noise terms $\{\epsilon_{i,j}\}$, is estimated at each grid point of a 1° resolution horizontal grid and at each pressure level, using all measurements (across depth) of the profiles located within 1,100 kilometers of the target grid point via likelihood-based estimation. Posterior inference at any given spatio-temporal point is then performed using the fitted local model corresponding to its nearest grid point and the subset of responses within 1,100 kilometers of the grid point horizontally.

Both approaches rely on complex mean structures and require sequential estimation of the mean field and the anomaly field. This two-stage modeling decouples mean estimation from anomaly inference, so uncertainty from the anomaly inference is not propagated to the original measurements. Furthermore, making inference based on the model estimated for the nearest grid point is sensitive to users' choice of grid density and the window size that the local model is based on. It also ignores long-range dependence and increases the risk of overfitting. These limitations motivate a principled, fully data-driven approach, which we introduce in the following section.

3 Principled GP modeling for Argo Temperature

In this section, we propose to apply a one-stop GP regression to the temperature variable in the Argo dataset to demonstrate that a direct, probabilistically principled GP regression can achieve comparable and in some cases, even better, results than representative methods in the literature that rely on prescribed mean structures, spatial partitions, and two-stage

modeling. Our method is also applicable to other Argo variables while we choose the temperature because it is the most widely used in the literature, hence aligning with our goal of providing a systematic comparison.

3.1 GP regression under ARD covariance functions

Gaussian processes (GPs) are a family of nonparametric stochastic models defined by a mean function $\mu(\cdot)$ and a covariance function $C(\cdot, \cdot)$. Specifically, for a collection of n points $\{\mathbf{s}_i \in \mathcal{D}\}_{i=1}^n$, where \mathcal{D} is the q -dimensional domain over which a GP is defined, their corresponding response variables $\mathbf{z} = [z_1, z_2, \dots, z_n]^\top$ jointly follow a multivariate normal (MVN) distribution:

$$\mathbf{z} \sim \mathcal{N}(\boldsymbol{\mu}, \boldsymbol{\Sigma}), \quad \boldsymbol{\mu} = [\mu(\mathbf{s}_1), \dots, \mu(\mathbf{s}_n)]^\top, \quad \text{and} \quad \boldsymbol{\Sigma}_{i,j} = C(\mathbf{s}_i, \mathbf{s}_j).$$

In this paper, we assume a constant mean function $\mu(\cdot) = \mu$ and a Matérn covariance function (Stein, 1999). Notice that Matérn covariance functions include the exponential covariance function used in Kuusela and Stein (2018) and Yarger et al. (2022) as a special case when the smoothness parameter is equal to 0.5. We further enhance the Matérn covariance function with an ARD structure, which leads to the covariance function:

$$C(\mathbf{s}_i, \mathbf{s}_j; \boldsymbol{\theta}) = \sigma^2 2^{1-\nu} / \Gamma(\nu) (\|\mathbf{R}^{-1}(\mathbf{s}_i - \mathbf{s}_j)\|)^\nu K_\nu(\|\mathbf{R}^{-1}(\mathbf{s}_i - \mathbf{s}_j)\|), \quad (7)$$

where $\mathbf{R} = \text{diag}(r_1, r_2, \dots, r_q)$ is a $q \times q$ diagonal matrix, with r_i^{-1} being the (positive) scaling factor of the i -th dimension of \mathcal{D} ; K_ν is the modified Bessel function of the second kind with smoothness ν ; and Γ is the gamma function. Notice that $\|\cdot\|$ is the Euclidean norm as the Matérn covariance function is not guaranteed positive-definite under other forms of distances. The ARD structure accounts for anisotropy by allowing separate lengthscales for the q domain dimensions, thereby providing extra flexibility while controlling the risk of overfitting assuming $n \gg q$. To summarize, our parameterization of GP involves one mean

parameter μ and the covariance parameters $\boldsymbol{\theta} = (\sigma^2, r_1, r_2, \dots, r_q, \nu)$.

The conventional method for estimating GP parameters is through MLE, where one needs to iteratively compute the log-likelihood of the GP realization over n locations. Given $\mathbf{z} \sim \mathcal{N}(\boldsymbol{\mu}, \boldsymbol{\Sigma})$, the likelihood for \mathbf{z} is

$$f(\mathbf{z}) = ((2\pi)^n |\boldsymbol{\Sigma}|)^{-1/2} \exp\left(-\frac{1}{2}(\mathbf{z} - \boldsymbol{\mu})^\top \boldsymbol{\Sigma}^{-1}(\mathbf{z} - \boldsymbol{\mu})\right), \quad (8)$$

where $|\boldsymbol{\Sigma}|$ denotes the determinant of $\boldsymbol{\Sigma}$. In practice, the matrix-inverse and the determinant are computed through the Cholesky factorization of the $n \times n$ covariance matrix $\boldsymbol{\Sigma}$, which requires $\mathcal{O}(n^2)$ memory and $\mathcal{O}(n^3)$ time. Consequently, the conventional method for estimating GP is limited to realizations over a few thousands of locations, for which, many scalable approximations for the GP likelihood were proposed. In this paper, we use the Vecchia approximation introduced in the next section.

3.2 The Vecchia approximation for Gaussian processes

The Vecchia approximation (Vecchia, 1988) decomposes an n -dimensional joint density into a product of univariate conditional densities and truncates the conditioning sets to sizes controlled by a tuning parameter m that only grows polylogarithmically with n , hence achieving an overall quasi-linear complexity with respect to n . Specifically, for a random vector $\mathbf{z} = [z_1, \dots, z_n]^\top$:

$$f(\mathbf{z}) = f(z_1) \prod_{i=2}^n f(z_i | \mathbf{z}_{1:i-1}) \approx f(z_1) \prod_{i=2}^n f(z_i | \mathbf{z}_{c(i)}), \quad (9)$$

where for each $i \in \{2, \dots, n\}$, the conditioning set $c(i)$ is a subset of $\{1, \dots, i-1\}$ and the cardinality of $c(i)$ is $\min(i-1, m)$. Choosing m between 30 and 50 has been shown (e.g. by Katzfuss et al. (2022); Datta et al. (2016); Cao et al. (2023),) to achieve sufficiently high accuracy for n on the magnitudes of tens of thousands under commonly used spatial covariance kernels. The ordering and the choice of the conditioning sets are the two tuning

factors of the Vecchia approximation. For improved accuracy, Guinness (2018) suggested using maximin ordering for higher accuracy while Katzfuss et al. (2022) proposed to choose the conditioning sets as the m nearest neighbors in the scaled domain, where the k -th dimension of \mathcal{D} is scaled by r_k^{-1} , both of which have established algorithms that have quasi-linear complexity with respect to n .

Technically, the Vecchia approximation is applicable to beyond MVN densities but here in this paper, we mainly consider the cases where $f(\mathbf{z})$ is a MVN density function, under which its Vecchia approximation, denoted by $\hat{f}(\mathbf{z})$, amounts to another MVN distribution with the same mean parameter but a slightly different covariance matrix, denoted by $\hat{\Sigma}$. Denoting the Cholesky factor and the inverse Cholesky factor of $\hat{\Sigma}$ by $\hat{\mathbf{L}}$ and $\hat{\mathbf{U}} = \hat{\mathbf{L}}^{-\top}$, respectively, $\hat{\mathbf{U}}$ is an upper triangular matrix whose non-zero off-diagonal entries in the j -th column are exactly indexed by $c(j)$. Therefore, $\hat{\mathbf{U}}$ is a sparse matrix with no more than nm non-zero entries and furthermore, $\hat{\mathbf{U}}$ can be computed in $\mathcal{O}(nm^3)$ time with straightforward parallelization over n (Katzfuss and Guinness, 2021). The GP likelihood function under the Vecchia approximation can be represented as:

$$\hat{f}(\mathbf{z}) = (2\pi)^{-n/2} |\hat{\mathbf{U}}| \exp\left(-\frac{1}{2} \|(\mathbf{z} - \boldsymbol{\mu})^\top \hat{\mathbf{U}}\|^2\right), \quad (10)$$

where $|\cdot|$ denotes the determinant and $\|\cdot\|^2$ denotes the square of the L^2 norm.

The Vecchia approximation also sheds light on the posterior inference at unobserved locations. Conventionally, the GP prediction at unobserved locations requires a one-time $\mathcal{O}(n^3)$ Cholesky factorization of Σ , followed by matrix-vector multiplications of complexity $\mathcal{O}(n^2)$ for each new prediction. In the framework of the Vecchia approximation, one can make prediction for z^* , the measurement at a new location \mathbf{s}^* , using only the m nearest neighbors of \mathbf{s}^* , essentially assuming $f(z^*|\mathbf{z}) \approx f(z^*|\mathbf{z}_{c^*})$, where $c^* \subset \{1, \dots, n\}$ is the set of indices of the m nearest neighbors of \mathbf{s}^* , hence achieving an $\mathcal{O}(m^3)$ complexity for the prediction at each new location, with $m \ll n$.

In summary, the Vecchia approximation reduces the computational cost of GP regression and inference to quasi-linear complexity in the number of training measurements n , while allowing straightforward parallelization over n . We fully leverage these advantages in applying GP regression to the large-scale Argo dataset.

3.3 One-stop GP regression

We propose to model an Argo variable of interest, for example, the temperature variable, using a one-stop GP regression, with the covariance function and the likelihood approximation introduced in Sections 3.1 and 3.2, respectively, avoiding the complexities of mean function parameterization or domain partition. Denote by W the Argo variable, we assume that within a wide spatial region,

$$W \sim \mathcal{GP}(\mu, C(\mathbf{s}_i, \mathbf{s}_j; \boldsymbol{\theta}) + \tau^2 \mathbb{1}_{\{\mathbf{s}_i = \mathbf{s}_j\}}), \quad (11)$$

where μ is the constant mean, C is the covariance function with parameter $\boldsymbol{\theta}$, $\tau^2 > 0$ denotes the nugget variance and $\mathbb{1}$ is the indicator function.

As in Yarger et al. (2022), we define the dimensions of the domain \mathcal{D} to include the latitude l , the longitude L , the pressure p , the year y , and the day of the year d . At a given latitude, longitudes of 180°E ($L = 180$) and 180°W ($L = -180$) correspond to the same physical location. Therefore, we represent the circular variable L using $L_s = \sin(\pi L/180)$ and $L_c = \cos(\pi L/180)$. To account for seasonality and ensure continuity between December and January, we similarly transform d into $d_s = \sin(2\pi d/365)$ and $d_c = \cos(2\pi d/365)$. Thus, each input vector is seven-dimensional, $\mathbf{s} = (l, L_s, L_c, p, y, d_s, d_c)$. For benchmarking experiments restricted to a single month (aggregated over multiple years), we omit d_s and d_c , assuming strong intra-month temporal correlation and favoring model parsimony.

Our proposed one-stop model estimation jointly optimizes μ , $\boldsymbol{\theta}$, and τ^2 via MLE, involving a total of eight or ten parameters. The Argo dataset is collected by approximately

4,000 floats, which together provide about 13,000 profiles per month, each containing an average of 200 measurements, resulting in over 30 million measurements annually for each Argo variable. This massive data volume renders exact GP-based MLE computationally prohibitive, even with the Vecchia approximation. To assess scalability and performance, we apply the proposed one-stop GP regression to subsets of the Argo dataset containing about 30,000 profiles and compare results against representative methods from the literature. The full suite of the Vecchia approximation procedures, including spatio-temporal input ordering, nearest-neighbor search for conditioning sets, log-likelihood computation, and the Fisher scoring algorithm for optimization, is implemented in the `GpGp` R package (Guinness, 2018). We set $m = 30$ for GP regression and $m = 100$ for posterior inference at testing locations.

4 Numerical Comparison

4.1 Experiment setup

In the following experiments, we use the Argo temperature data collected from January to March over the years from 2007 to 2016 to compare our proposed one-stop GP to the moving-window GP regression (MWGP) from Kuusela and Stein (2018) and the spatio-temporal kriging for functional data (KFD) from Yarger et al. (2022). We use the pre-screened Argo data as in Kuusela and Stein (2018), where measurements deemed contaminated are removed. Both Kuusela and Stein (2018) and Yarger et al. (2022) demonstrated their performances by predicting the Argo temperature in February, with the former proposing two models addressing using either the same month’s (i.e., February’s) or the whole three months’ data for training, respectively. For a more comprehensive comparison, we also set up two training scenarios, using only February’s or all three months’ temperature measurements from the training profiles for model estimation, to predict February’s temperature measurements of the testing profiles.

The two time windows, February alone and January through March, correspond to 73,534

and 234,401 profiles, respectively, over the years 2007–2016, rendering direct numerical comparison computationally infeasible. We downsampled the data to 30,000 profiles using three different strategies: one global and two regional, forming three distinct training–testing scenarios. The global subset includes floats distributed worldwide, while the two regional subsets each comprises floats within a 4,250-kilometer radius—one centered in the open Pacific Ocean and the other in the Atlantic Ocean, capturing more coastal observations. The profiles in each scenario are then randomly split into 80% for training and 20% for testing. To ensure consistency with Kuusela and Stein (2018) and Yarger et al. (2022), we further downscale the testing profiles to those collected in Februaries. Besides the selection of profiles, Kuusela and Stein (2018) and Yarger et al. (2022) both considered measurements of profiles localized to three pressure levels, namely 10, 300, and 1,500 dbar, covering the depth ranges of [5, 15] dbar, [290, 310] dbar, and [1450, 1550] dbar, respectively. Following their approach, we also subset the measurements of the profiles within each training–testing scenario into these three depth bins, yielding nine datasets in total. Datasets corresponding to the pressure levels 10 dbar and 300 dbar each has approximately 80,000 measurements in the training set and 6,500 measurements in the testing set, while those corresponding to 1,500 dbar each has approximately 200,000 measurements in the training set and 16,000 measurements in the testing set.

Both Kuusela and Stein (2018) and Yarger et al. (2022) used localized methods in their estimations of the mean structure and the subsequent estimations of the anomaly field. However, the two methods differ in terms of their mean structure parameterizations, sizes of domain partitions, and the resolution of their chosen horizontal grids; please refer to Section 2 for more details. When implementing the MWGP method, we compute the RG mean field (1) at each $1/6^\circ \times 1/6^\circ$ horizontal grid point for each month from January to March at the three pressure levels, using the whole three-month training dataset across depth, resulting in nine mean fields in total. MWGP further estimated local covariance parameters via MLE using training-profile anomalies within a $20^\circ \times 20^\circ$ moving window centered at each 1°

ocean grid point. Kuusela and Stein (2018) tested the MWGP method with two different covariance parameterizations, corresponding to their Models 2 and 5, respectively. Specifically, the former considers only spatial correlation, defining two range parameters r_l and r_L for longitude and latitude, respectively, while the latter also considered temporal correlation by including an extra range parameter r_d for ‘day of the year’. The prediction for the testing profiles at the target pressure level was the sum of the mean predictions and the anomaly kriging results. The two models are denoted by MWGP-S and MWGP-ST, respectively, in this paper. For the KFD method, the functional mean with depth-varying coefficients (5) is locally estimated at each $1^\circ \times 1^\circ$ (horizontal) grid point, using January–March training profiles located within 900 km of that point. Subsequently, analogous to the $20^\circ \times 20^\circ$ moving-window approach, the mean-subtracted training anomalies within 1,100 km of each grid point are used to locally estimate the covariance structures of the stochastic process ξ and the functional nugget ϵ in Equation (4). It is worth noting that our implementations of Kuusela and Stein (2018) and Yarger et al. (2022) have minor differences from their original implementations. Kuusela and Stein (2018) and Yarger et al. (2022) estimated the mean structures using data from both training and testing profiles, incorporating temperature measurements across all depths, before dividing the resulting anomalies into pressure bins for kriging. To align with our training-testing setup, we follow their procedure for mean estimation using measurements across depths but apply it to data from the training profiles only. Notice that due to the usage of weighted least square regression in Kuusela and Stein (2018) and Yarger et al. (2022), the fitted mean structures are different at the three pressure levels even using the same collection of training profiles.

Our proposed one-stop GP directly maximizes the GP log-likelihood over the training profiles at the target depth for each of the nine training-testing scenarios, not involving the complexities of domain partitioning or mean structure estimation described above. We use a Matérn covariance kernel while optimizing the collection of parameters of μ , τ^2 , and $\boldsymbol{\theta} = (\sigma^2, r_1, r_2, \dots, r_7, \nu)$, where r_1, r_2, \dots, r_7 correspond to $(l, L_s, L_c, p, y, d_s, d_c)$ as introduced in

Section 3.3. We refer to this model as GP-7D. When only profiles in Februaries were used for training, we considered a slightly modified GP that omitted d_s and d_c , referred to as GP-5D. The GPs trained with only the profiles in Februaries are used for comparison with the MWGP-S from Kuusela and Stein (2018) while those trained with all three months’ profiles are compared against MWGP-ST as well as the KFD method.

The criteria we use to compare the posterior inference made by different methods are: the root-mean-square error (RMSE), the third quartile of the absolute error (Q3AE), the median absolute error (MdAE), the mean absolute error (MAE), the continuous ranked probability score (CRPS), and the coefficient of determination (R^2). RMSE is the most commonly used performance metric while Q3AE, MdAE, and MAE were used in Kuusela and Stein (2018) and Yarger et al. (2022) and hence are also included here. CRPS is defined as

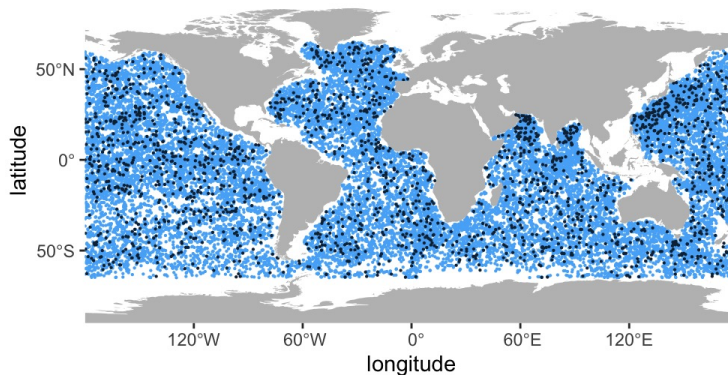
$$\text{CRPS} = \frac{1}{N} \sum_{p=1}^N \left(\int_{-\infty}^{W(\mathbf{s}_p^*)} (\Phi_p^*(x))^2 dx + \int_{W(\mathbf{s}_p^*)}^{\infty} (1 - \Phi_p^*(x))^2 dx \right), \quad (12)$$

where $W(\mathbf{s}_p^*)$ is the observed temperature at prediction location \mathbf{s}_p^* , N is the number of measurements in the testing dataset, and $\Phi_p^*(\cdot)$ is the cumulative distribution function of the prediction distribution, which is typically assumed normal. CRPS measures the quality of both point prediction and uncertainty quantification while R^2 shows the prediction error relative to the total variation. Notice that the magnitudes of the Argo variables, including the temperature, varies substantially with depth and typically, the variance in depth bins closer to the surface are much higher, for which the R^2 contributes to a more comprehensive comparison.

4.2 The Global scenario

From the profiles collected over the three-month period of January to March from 2007 to 2016, we randomly select 30,000 profiles, with their spatial locations shown in Figure 1. Of these, 80% and 20% are randomly assigned to the training and testing sets, respectively,

Figure 1: Locations of the 30,000 profiles in the ‘global’ subset that are selected from the 234,401 profiles over the period of January to March, 2007–2016. The profiles in the training set are marked in blue, and the profiles in the testing set are marked in black.

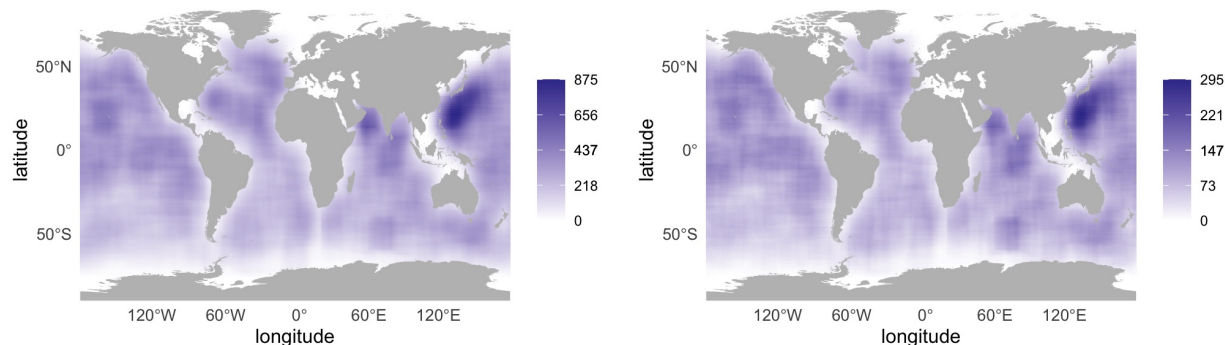


with the testing profiles further restricted to those collected in February. Figure 2a presents the density of training profiles, measured by the number of profiles in each $20^\circ \times 20^\circ$ moving-window, which is the same window size as used by Kuusela and Stein (2018) for modeling and predicting the anomaly field. Except for the Philippine Sea and the Arabian Sea, the density of training profiles is relatively low compared with the profile densities used in the benchmark works of Kuusela and Stein (2018) and Yarger et al. (2022), with each $20^\circ \times 20^\circ$ window containing approximately 400 profiles over the three-month period. The density distribution of training profiles in February follows the same pattern as that of the three-month training data, but differing by a factor 1/3.

The predictive performance of the three methods, namely MWGP, KFD, and the proposed one-stop GP, is summarized in Table 1. Overall, the one-stop GP consistently outperforms the other approaches, except at the 10 dbar pressure level under the three-month window, where the functional model of Yarger et al. (2022) achieves slightly better results. All methods yield satisfactory R^2 values, demonstrating their effectiveness for globally distributed Argo profiles despite the sparse spatial coverage of the training data. The model rankings remained consistent across all evaluation criteria: lower RMSE values were generally accompanied by smaller absolute error metrics (Q_3 AE, MdAE, and MAE), higher R^2 ,

Figure 2: The number of training profiles within a $20^\circ \times 20^\circ$ moving-window centered at each grid point of a 1° resolution horizontal grid.

(a) Training profile density during January to March (b) Training profile density during February



and lower CRPS. This agreement across metrics indicated that the observed performance improvements were consistent in point prediction accuracy and uncertainty quantification. Unlike MWGP and KFD, which assumed the exponential covariance function that essentially fixed the Matérn smoothness at 0.5, our one-stop GP estimated it directly, leveraging the computational efficiency of the Vecchia approximation. The estimated smoothness ranged from 0.4 to 0.9, with higher values at deeper levels (e.g., 1,500 dbar), reflecting smoother variability with depth. This flexibility contributed to the superior performance of the one-stop GP summarized in Table 1.

When the training profiles were limited to February, GP-5D occasionally outperformed GP-7D, suggesting mild overfitting in the latter and highlighting the benefit of model parsimony. Expanding the training window to three months improved the performance of both MWGP and GP-7D, reflecting their data efficiency, with more pronounced gains for the one-stop GP. In particular, at 300 dbar and 1,500 dbar, the one-stop GP achieved over a 13% reduction in RMSE, whereas MWGP-ST improved upon MWGP-S by less than 10%, underscoring the one-stop GP’s superior ability to capture temporal correlation. In principle, the one-stop GP can jointly model profiles across multiple depth levels, not requiring the datasets are measured at the same depth level, for which we also tried fitting the one-stop GP to the training profiles across depth and used the trained model to predict the testing profiles

Table 1: Model performance comparison in predicting the temperature measurements at selected pressure levels from the testing profiles in the global experiment scenario. The first column shows the month-depth pair, with depth having the unit of dbar. For each scenario, the best value of each performance metric is indicated in **bold**.

Data	Model	RMSE	Q ₃ AE	MdAE	MAE	R^2	CRPS
Feb - 10	MWGP-S	0.8712	0.7725	0.4115	0.5843	0.9896	0.4540
	GP-7D	0.8250	0.7301	0.3757	0.5521	0.9915	0.4162
	GP-5D	0.8483	0.7516	0.3908	0.5671	0.9910	0.4271
Jan-Mar - 10	MWGP-ST	0.8186	0.7142	0.3785	0.544	0.9909	0.3962
	KFD	0.6806	0.6294	0.3101	0.4604	0.9944	0.3379
	GP-7D	0.8238	0.7792	0.4005	0.569	0.9915	0.4282
Feb - 300	MWGP-S	0.9934	0.8631	0.4076	0.6462	0.9502	0.5182
	GP-7D	0.9747	0.7780	0.3659	0.6128	0.9569	0.4832
	GP-5D	0.9043	0.7343	0.3391	0.5652	0.9629	0.4443
Jan-Mar - 300	MWGP-ST	0.9362	0.8158	0.4016	0.6224	0.9558	0.4539
	KFD	0.8355	0.6634	0.3571	0.5325	0.9684	0.3895
	GP-7D	0.7763	0.6351	0.2828	0.4891	0.9727	0.3863
Feb - 1500	MWGP-S	0.1698	0.1497	0.0737	0.1133	0.9702	0.0927
	GP-7D	0.1419	0.1301	0.0674	0.0986	0.9793	0.0752
	GP-5D	0.1344	0.1213	0.0608	0.0912	0.9814	0.0702
Jan-Mar - 1500	MWGP-ST	0.1529	0.1359	0.0708	0.1041	0.9765	0.0750
	KFD	0.1313	0.1158	0.0567	0.0873	0.9823	0.0698
	GP-7D	0.1165	0.1052	0.0527	0.0797	0.9861	0.0605

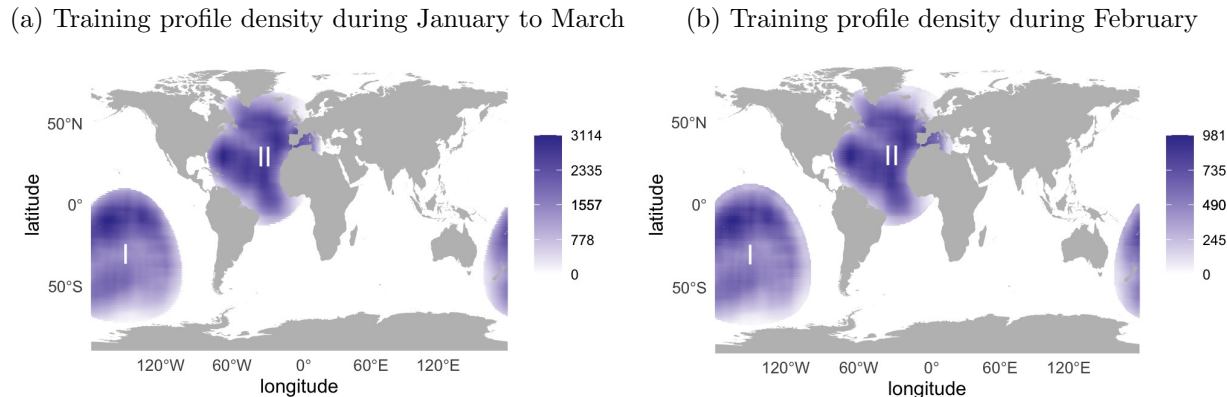
at the designated depth levels. We tested this capability by fitting a single GP-7D across all depths and predicting at designated pressure levels. The results were mixed: R^2 slightly improved at 300 and 1,500 dbar but declined at 10 dbar, consistent with the known vertical nonstationarity of the Argo data (Roemmich and Gilson, 2009; Gasparin et al., 2015), which may call for more sophisticated covariance constructions.

4.3 The Regional scenarios

For the two regional training–testing experiments, we selected profile subsets within 4,250 km of (30°S, 150°W) and (30°N, 30°W), respectively, resulting in approximately 30,000 profiles per region, about 10,000 of which were collected in February. Figures 3a–3b display the number of training profiles within each $20^\circ \times 20^\circ$ moving window centered on a $1^\circ \times 1^\circ$ grid across the study domains. While the global experiment in Section 4.2 used a lower

profile density than those in Kuusela and Stein (2018) and Yarger et al. (2022), the regional experiments matched their data densities. Consequently, these regional analyses more closely mirror the data configurations of Kuusela and Stein (2018) and Yarger et al. (2022), making the performance of MWGP and KFD more representative of their original implementations. Notably, reducing the spatial domain for MWGP and KFD training had little effect on their performances, as both methods rely on local model estimation or prediction based on smaller spatial partitions. For the one-stop GP, the estimated smoothness parameters differed from those in the global experiment. In the region centered at $(30^\circ\text{S}, 150^\circ\text{W})$, the smoothness for GP-5D was approximately 0.2, increasing slightly at the 1,500 dbar pressure level. For GP-7D, the smoothness was around 0.4 at 10 and 1,500 dbar, and about 0.2 at 300 dbar. In contrast, in the region centered at $(30^\circ\text{N}, 30^\circ\text{W})$, the estimated smoothness values were more stable—about 0.5 for GP-7D and 0.4 for GP-5D across all three pressure levels.

Figure 3: The number of training profiles within a $20^\circ \times 20^\circ$ moving-window centered at each grid point of a 1° resolution horizontal grid over selected regions. Region I is centered at $(30^\circ\text{S}, 150^\circ\text{W})$, corresponding to Table 2; Region II is centered at $(30^\circ\text{N}, 30^\circ\text{W})$, corresponding to Table 3.



The performance comparisons for the two regional scenarios are summarized in Tables 2 and 3, where the one-stop GP generally outperformed all competing methods. Specifically, it achieved 4 and 5 best scores out of 6 scenarios in Tables 2 and 3, respectively. The one-stop GP showed greater improvement over MWGP and KFD at deeper pressure levels, likely reflecting stronger nonstationarity in shallow waters and smoother temperature variations at

Table 2: Model performance comparison in predicting the temperature measurements at selected pressure levels from the testing profiles in the region centered at (30°S, 150°W). The first column shows the month-depth pair, with depth having the unit of dbar. For each scenario, the best value of every evaluation criterion is indicated in **bold**.

Data	Model	RMSE	Q ₃ AE	MdAE	MAE	R ²	CRPS
Feb - 10	MWGP-S	0.5728	0.5713	0.3060	0.4167	0.9950	0.3827
	GP-5D	0.5474	0.5315	0.2770	0.3835	0.9958	0.2855
	GP-7D	0.6964	0.7229	0.4073	0.5224	0.9932	0.3849
Jan-Mar - 10	MWGP-ST	0.4235	0.4092	0.1947	0.2927	0.9973	0.2137
	KFD	0.4536	0.4104	0.2084	0.3116	0.9973	0.2499
	GP-7D	0.4743	0.4197	0.1994	0.3137	0.9968	0.2378
Feb - 300	MWGP-S	0.6038	0.5794	0.2832	0.4228	0.9797	0.3896
	GP-5D	0.5508	0.5065	0.2338	0.3733	0.9832	0.2896
	GP-7D	0.5654	0.5271	0.2409	0.3856	0.9823	0.2988
Jan-Mar - 300	MWGP-ST	0.4874	0.4675	0.2212	0.3341	0.9861	0.2472
	KFD	0.4546	0.4147	0.2041	0.3110	0.9889	0.2599
	GP-7D	0.4771	0.4486	0.2040	0.3233	0.9874	0.2494
Feb - 1500	MWGP-S	0.0813	0.0737	0.0396	0.056	0.9594	0.0418
	GP-5D	0.0784	0.0708	0.0394	0.0535	0.9746	0.0398
	GP-7D	0.0914	0.0811	0.0414	0.0611	0.9655	0.0473
Jan-Mar - 1500	MWGP-ST	0.0814	0.0769	0.0420	0.0569	0.9577	0.0414
	KFD	0.0771	0.0677	0.0338	0.0498	0.9765	0.0464
	GP-7D	0.0649	0.0604	0.0331	0.0449	0.9826	0.0335

greater depths. Compared with the global results in Table 1 (Section 4.2), MWGP-ST exhibited significantly better performance, suggesting that it benefited from the higher density of training floats in regional subsets. In both regional cases, GP-5D consistently outperformed MWGP-S, underscoring the advantage of nonparametric GP models over parametric regression approaches. Furthermore, when training profiles were restricted to those collected in February, GP-7D consistently underperformed GP-5D, highlighting the importance of selecting informative covariates and maintaining model parsimony. Finally, prediction accuracy at 10 dbar and 300 dbar was higher in the region centered at (30°S, 150°W) than in the region centered at (30°N, 30°W), likely due to greater temperature variability in coastal regions at shallow depths.

It is noteworthy that the rankings based solely on point prediction accuracy did not always align with those incorporating both prediction and uncertainty quantification. For

Table 3: Model performance comparison in predicting the temperature measurements at selected pressure levels from the testing profiles in the region centered at (30°N, 30°W). The first column shows the month-depth pair, with depth having the unit of dbar. For each scenario, the best value of every evaluation criterion is indicated in **bold**.

Data	Model	RMSE	Q ₃ AE	MdAE	MAE	R ²	CRPS
Feb - 10	MWGP-S	0.8093	0.4408	0.2195	0.4155	0.9881	0.3399
	GP-5D	0.7362	0.4355	0.2111	0.3845	0.9908	0.3157
	GP-7D	0.8086	0.5661	0.2716	0.4636	0.9889	0.3740
Jan-Mar - 10	MWGP-ST	0.6528	0.3194	0.1525	0.3092	0.9922	0.2389
	KFD	0.5603	0.3333	0.1688	0.2995	0.9947	0.2426
	GP-7D	0.5348	0.3181	0.1427	0.2831	0.9951	0.2415
Feb - 300	MWGP-S	0.7555	0.4206	0.1826	0.3852	0.9661	0.3238
	GP-5D	0.7411	0.4264	0.194	0.3859	0.9712	0.3160
	GP-7D	0.7436	0.4282	0.194	0.3853	0.9711	0.3315
Jan-Mar - 300	MWGP-ST	0.5836	0.3505	0.1575	0.2987	0.9793	0.2322
	KFD	0.6368	0.3651	0.1728	0.3348	0.9787	0.2610
	GP-7D	0.6459	0.368	0.1619	0.3275	0.9782	0.2708
Feb - 1500	MWGP-S	0.2148	0.1412	0.0667	0.1226	0.9863	0.1013
	GP-5D	0.1606	0.1157	0.0549	0.0962	0.9867	0.0763
	GP-7D	0.1621	0.1155	0.0547	0.0968	0.9864	0.0776
Jan-Mar - 1500	MWGP-ST	0.1596	0.1235	0.0571	0.0985	0.9924	0.0731
	KFD	0.1494	0.1096	0.0554	0.0888	0.9890	0.0939
	GP-7D	0.1226	0.0939	0.0451	0.0751	0.9922	0.0589

instance, at the 300 dbar pressure level in the region centered at (30°S, 150°W), MWGP-ST achieved the lowest CRPS, whereas KFD performed best on other metrics, revealing KFD’s deficiency in uncertainty quantification in certain scenarios. In contrast, the one-stop GP, being a principled likelihood-based method, typically provides more reliable estimates of predictive uncertainty.

5 Conclusion

In this paper, we propose a one-stop Gaussian process (GP) regression framework for modeling the Argo dataset, addressing the ad hoc nature of commonly used approaches that rely on domain partitioning and two-stage optimization. The vast scale of the Argo data presents significant computational challenges for classical GP regression, whose com-

putational cost scales cubically with the number of measurements n . To overcome this, we employ the Vecchia approximation (Vecchia, 1988), which reduces the computational complexity of the likelihood and its gradient to quasi-linear in n . Although GP regression under the Vecchia approximation has been well studied (e.g. by Katzfuss and Guinness (2021); Katzfuss et al. (2022); Cao et al. (2024, 2022)), our work demonstrates that GPs, as non-parametric models, can be effectively applied to the Argo dataset without requiring complex parametric mean structures. Moreover, we highlight the advantages of the Vecchia approximation in substantially enhancing scalability, thereby eliminating the need for partition-wise independence, an assumption that neglects long-range correlations, increases susceptibility to overfitting, and introduces discontinuities across boundaries.

We compare our approach with two representative methods in the literature: the moving-window GP regression of Kuusela and Stein (2018) and the spatio-temporal kriging for functional data method of Yarger et al. (2022). Both methods estimate prescribed mean structures via weighted least squares, followed by local GP regression for mean-subtracted anomalies. These two-stage procedures raise methodological concerns regarding the choice of domain partitions and the specification of parametric mean structures. Both choices are sensitive to dataset characteristics such as spatial coverage, temporal span, and depth range, leading to ambiguity and reduced reproducibility for practitioners. In contrast, our one-stop GP regression achieves superior overall performance compared with Kuusela and Stein (2018) and Yarger et al. (2022) on the same Argo datasets, offering an off-the-shelf, principled, and interpretable modeling tool for oceanographic applications.

A promising direction for future research is the development of nonstationary covariance structures to better capture the pronounced nonstationarity of the Argo data, particularly along the depth dimension. In this context, while the Vecchia approximation is essential for scalability, its integration with nonstationary covariance functions remains underexplored—primarily due to the challenges in constructing conditioning sets. Addressing this limitation represents a key opportunity for advancing scalable, flexible GP modeling of

large-scale oceanographic datasets.

6 Acknowledgment

The authors acknowledge the support from the University of Houston, which provided the resources and environment that facilitated this research. We would also like to thank Drew Yarger for sharing resources that supported our replication of the method in Yarger et al. (2022). These Argo data were collected and made freely available by the International Argo Program and the national programs that contribute to it. (<https://argo.ucsd.edu>, <https://www.ocean-ops.org>). The Argo Program is part of the Global Ocean Observing System.

References

- [1] Argo (2000). Argo float data and metadata from Global Data Assembly Centre (Argo GDAC). <https://doi.org/10.17882/42182>.
- [2] Bevilacqua, M., Gaetan, C., Mateu, J., and Porcu, E. (2012). Estimating space and space-time covariance functions for large data sets: a weighted composite likelihood approach. *Journal of the American Statistical Association*, 107(497):268–280.
- [3] Bolin, D. and Wallin, J. (2020). Multivariate type g matérn stochastic partial differential equation random fields. *Journal of the Royal Statistical Society Series B: Statistical Methodology*, 82(1):215–239.
- [4] Bretherton, F. P., Davis, R. E., and Fandry, C. (1976). A technique for objective analysis and design of oceanographic experiments applied to mode-73. *Deep Sea Research and Oceanographic Abstracts*, 23(7):559–582.
- [5] Cao, J., Guinness, J., Genton, M. G., and Katzfuss, M. (2022). Scalable Gaussian-process

- regression and variable selection using Vecchia approximations. *Journal of Machine Learning Research*, 23(348):1–30.
- [6] Cao, J., Kang, M., Jimenez, F., Sang, H., Schaefer, F. T., and Katzfuss, M. (2023). Variational Sparse Inverse Cholesky Approximation for Latent Gaussian Processes via Double Kullback-Leibler Minimization. In *Proceedings of the 40th International Conference on Machine Learning*, pages 3559–3576. PMLR. ISSN: 2640-3498.
- [7] Cao, J., ZHANG, J., SUN, Z., and Katzfuss, M. (2024). Locally Anisotropic Non-stationary Covariance Functions on the Sphere. *Journal of Agricultural, Biological and Environmental Statistics*, 29(2):212–231.
- [8] Datta, A., Banerjee, S., Finley, A. O., and Gelfand, A. E. (2016). Hierarchical nearest-neighbor gaussian process models for large geostatistical datasets. *Journal of the American Statistical Association*, 111(514):800–812.
- [9] Du, J., Zhang, H., and Mandrekar, V. S. (2009). Fixed-domain asymptotic properties of tapered maximum likelihood estimators. *The Annals of Statistics*, 37(6A):3330–3361.
- [10] Eidsvik, J., Shaby, B. A., Reich, B. J., Wheeler, M., and Niemi, J. (2014). Estimation and prediction in spatial models with block composite likelihoods. *Journal of Computational and Graphical Statistics*, 23(2):295–315.
- [11] Finley, A. O., Datta, A., Cook, B. D., Morton, D. C., Andersen, H. E., and Banerjee, S. (2019). Efficient algorithms for bayesian nearest neighbor gaussian processes. *Journal of Computational and Graphical Statistics*, 28(2):401–414. PMID: 31543693.
- [12] Furrer, R., Genton, M. G., and Nychka, D. (2006). Covariance tapering for interpolation of large spatial datasets. *Journal of Computational and Graphical Statistics*, 15(3):502–523.

- [13] Gasparin, F., Roemmich, D., Gilson, J., and Cornuelle, B. (2015). Assessment of the upper-ocean observing system in the equatorial pacific: The role of argo in resolving intraseasonal to interannual variability. *Journal of Atmospheric and Oceanic Technology*, 32(9):1668 – 1688.
- [14] Gray, A. R. and Riser, S. C. (2015). A method for multiscale optimal analysis with application to argo data. *Journal of Geophysical Research: Oceans*, 120(6):4340–4356.
- [15] Guinness, J. (2018). Permutation and grouping methods for sharpening gaussian process approximations. *Technometrics*, 60(4):415–429.
- [16] Guinness, J. (2021). Gaussian process learning via Fisher scoring of Vecchia’s approximation. *Statistics and Computing*, 31(3):25.
- [17] Hu, A. J., Kuusela, M., Lee, A. B., Giglio, D., and Wood, K. M. (2024). Spatiotemporal methods for estimating subsurface ocean thermal response to tropical cyclones. *Advances in Statistical Climatology, Meteorology and Oceanography*, 10(2):69–93.
- [18] Katzfuss, M. (2017). A multi-resolution approximation for massive spatial datasets. *Journal of the American Statistical Association*, 112(517):201–214.
- [19] Katzfuss, M. and Guinness, J. (2021). A General Framework for Vecchia Approximations of Gaussian Processes. *Statistical Science*, 36(1):124–141. Publisher: Institute of Mathematical Statistics.
- [20] Katzfuss, M., Guinness, J., and Lawrence, E. (2022). Scaled Vecchia Approximation for Fast Computer-Model Emulation. *SIAM/ASA Journal on Uncertainty Quantification*, 10(2):537–554.
- [21] Kaufman, C. G., Schervish, M. J., and Nychka, D. W. (2008). Covariance tapering for likelihood-based estimation in large spatial data sets. *Journal of the American Statistical Association*, 103(484):1545–1555.

- [22] Korte-Stapff, M., Yarger, D., Stoev, S., and Hsing, T. (2022). A functional regression model for heterogeneous biogeochemical argo data in the southern ocean. <https://doi.org/10.48550/arXiv.2211.04012>. arXiv:2211.04012.
- [23] Kuusela, M. and Stein, M. L. (2018). Locally stationary spatio-temporal interpolation of argo profiling float data. *Proceedings of the Royal Society A: Mathematical, Physical and Engineering Sciences*, 474.
- [24] Lindgren, F., Rue, H., and Lindström, J. (2011). An explicit link between gaussian fields and gaussian markov random fields: the stochastic partial differential equation approach. *Journal of the Royal Statistical Society: Series B (Statistical Methodology)*, 73(4):423–498.
- [25] Neal, R. M. (2012). *Bayesian learning for neural networks*, volume 118. Springer Science & Business Media.
- [26] Nychka, D., Bandyopadhyay, S., Hammerling, D., Lindgren, F., and Sain, S. (2015). A multiresolution gaussian process model for the analysis of large spatial datasets. *Journal of Computational and Graphical Statistics*, 24(2):579–599.
- [27] Ridgway, K. R., Dunn, J. R., and Wilkin, J. L. (2002). Ocean interpolation by four-dimensional weighted least squares—application to the waters around australasia. *Journal of Atmospheric and Oceanic Technology*, 19(9):1357 – 1375.
- [28] Roemmich, D. (1983). Optimal estimation of hydrographic station data and derived fields. *Journal of Physical Oceanography*, 13(8):1544–1549.
- [29] Roemmich, D. and Gilson, J. (2009). The 2004–2008 mean and annual cycle of temperature, salinity, and steric height in the global ocean from the argo program. *Progress in Oceanography*, 82(2):81–100.
- [30] Rue, H. and Held, L. (2005). *Gaussian Markov random fields: theory and applications*. Chapman and Hall/CRC.

- [31] Salvana, M. L., Cao, J., and Jun, M. (2025). 3d bivariate spatial modelling of argo ocean temperature and salinity profiles. <https://doi.org/10.48550/arXiv.2210.11611>. arXiv:2210.11611.
- [32] Schäfer, F., Katzfuss, M., and Owhadi, H. (2021). Sparse cholesky factorization by kullback–leibler minimization. *SIAM Journal on scientific computing*, 43(3):A2019–A2046.
- [33] Stein, M. L. (1999). *Interpolation of Spatial Data*. Springer New York, NY.
- [34] Stein, M. L., Chi, Z., and Welty, L. J. (2004). Approximating Likelihoods for Large Spatial Data Sets. *Journal of the Royal Statistical Society Series B: Statistical Methodology*, 66(2):275–296.
- [35] Varin, C., Reid, N., and Firth, D. (2011). An overview of composite likelihood methods. *Statistica Sinica*, 21(1):5–42.
- [36] Vecchia, A. V. (1988). Estimation and Model Identification for Continuous Spatial Processes. *Journal of the Royal Statistical Society. Series B (Methodological)*, 50(2):297–312. Publisher: [Royal Statistical Society, Wiley].
- [37] Yarger, D. and Bhadra, A. (2023). Multivariate confluent hypergeometric covariance functions with simultaneous flexibility over smoothness and tail decay. <https://doi.org/10.48550/arXiv.2312.05682>. arXiv:2312.05682.
- [38] Yarger, D., Stoev, S., and Hsing, T. (2022). A functional-data approach to the Argo data. *The Annals of Applied Statistics*, 16(1):216 – 246.
- [39] Yarger, D., Stoev, S., and Hsing, T. (2023). Multivariate matérn models – a spectral approach. <https://doi.org/10.48550/arXiv.2309.02584>. arXiv:2309.02584.